

# VASCULAR JOURNEY AND ADHESION MECHANICS OF MICRO-SIZED CARRIERS IN NARROW CAPILLARIES

Alessandro Coclite<sup>1,b,\*</sup>

<sup>a</sup>*Scuola di Ingegneria, Università degli Studi della Basilicata, Potenza, Viale dell'Ateneo Lucano – 85100 Potenza, Italy*

<sup>b</sup>*Centro di Eccellenza in Meccanica Computazionale (CEMeC), Politecnico di Bari, Via Re David 200 – 70125 Bari, Italy*

---

## Abstract

Micro and nano-particles are systemically injected as drug carriers to specifically deliver therapeutics into diseased tissue. Their vascular journey and adhesion mechanics are key ingredient to optimize strategies mainly against cancer and cardiovascular disorders. This work focuses on the role of carrier stiffness in modulating their migration towards capillary peripheries and then to firmly adhere vascular walls. A Lattice Boltzmann-Immersed Boundary method is used for predicting the dynamics of rigid and deformable adhesive micro-metric particles ( $1\ \mu m$ ) navigating a capillary by the size of  $10\ \mu m$  with 20% hematocrit. Cells and microcarriers are modeled as a collection of mass-spring elements responding to a bending potential, a worm-like chain potential and the area conservation constraint. Furthermore, particle's surface is decorated with adhesive molecules interacting with vascular walls. Particles' transport and adhesion are characterized in terms of their ability to reach the capillary peripheries (margination rate) and to firmly adhere the vascular walls. This analysis is carried out systematically by varying particles' and cells' initial positions (five different particles configurations are transported, one per time, within four red blood cells releasing positions); stiffness (rigid  $Ca = 0$  and soft  $Ca = 10^{-2}$  particles are considered) and their chemical affinity with the capillary walls ( $\sigma = 0.5, 1$ , and  $2$ ). Particle stiffness is found to weekly influence the margination rate while do significantly affect the ability of such constructs to efficiently interact with the endothelium by forming stable chemical bonds.

*Keywords:*

## 1. INTRODUCTION

Micro- and nano-particles have been proven as efficient carriers of therapeutics for the specific treatment of diseases such as cancer or cardiovascular disorders. [1, 2] For the target specific delivery of drugs, two major steps are required: the accumulation of these small constructs into the capillary peripheries (*margination process*) and their adhesion to the diseased tissue. **In particular, the big challenge of soft nanomedicines is to selectively stick to capillary walls by taking the advantages of the capillary proliferation into inflamed regions. Then, once stably adhering the vasculature, to start the extravasation process while releasing their cargo.**

Computational methods are crucial to deep understand the vascular transport of platelets-like objects due to the large number of parameters involved. Particles can be precisely tailored in term of their shape, size, superficial properties and stiffness (the so called 4S parameters) to modulate their abilities, so that, the number of paths toward the optimization uncontrollably grows. [3, 4] In recent years, a number of scientists have studies blood flows analyzing the complex features related to the presence of red blood cells, platelets and cells into the margination of micro- and nanoparticles. [5–13] By definition, margination corresponds to the dislodging of immersed objects toward vessel walls. It has been observed experimentally for white blood cells, platelets and rigid microparticles, however the dependence of margination on particle's stiffness, shape, size, and surface properties remains an open question. [5, 14] Then, such carriers should stably adhere to the vessel walls in order to support the continuous and controlled release of drugs into the diseased tissue [15]. The recipe for efficient micro- and nano-carriers is far from being discovered

---

\*Corresponding author

Email address: `alessandro.coclite@unibas.it` (Alessandro Coclite)

and computational model are useful tools for the design of such constructs. Indeed, reliable computational schemes must account for the transport of several structures with different stiffnesses, densities, shapes, and need to model particle-particle and particle-walls interactions. [15, 16]

In this work, a kinematic/dynamics hybrid Immersed–Boundary (IB)/Lattice Boltzmann (LB) scheme is employed. [16] Precisely, the IB technique is employed in its kinematic formulation for the red blood cells in order to save computational time. Indeed, red cell membrane is considered here as dense as plasma, so that, the membranes velocity is advected with the withstanding fluid velocity. On the contrary, microparticles are transported in a  $10\ \mu m$  narrow capillary with the dynamics IB formulation extensively developed and validated by the author and collaborators. [15–18] Particles are chosen to be slightly denser than RBCs in order to mimic discoidal PLGA microparticles developed by Key et al. [19]. Such dynamics–IB scheme is adopted due to its ability to compute, within the same framework, rigid and deformable particles. Particle dynamics is predicted under different conditions, namely: four cell releasing positions; five particle initial configurations; two values for particle’s mechanical stiffness; and three values for the particle chemical affinity with the vascular walls. Firstly, the blood cells are transported alone, thus identifying three flow regions discriminated by the perturbation induced by their presence: a bulk region, RBC rich zone; an intermediate layer, fluid region in which the flow is only slightly perturbed by the cells peripheries; and a cell–free layer, unperturbed flow region. Then, particles are released into the fluid domain and the number of particles in time populating the three regions is computed. The margination ability of soft and rigid constructs is measured by counting the number of particles populating in time these three regions. Interestingly, for  $1\ \mu m$  construct the stiffness poorly affects the margination rate, while soft particles are more prone to firmly adhere the vasculature. As the matter of facts, only 6% of the total number of rigid particles can firmly adhere to the vasculature while this number grows up to 23% when considering soft membranes.

## 2. COMPUTATIONAL METHOD

### 2.1. TWO DIMENSIONAL BGK-LATTICE BOLTZMANN METHOD

The evolution of the fluid is defined in terms of a set of  $N$  discrete distribution functions,  $[f_i]$ , ( $i = 0, \dots, N-1$ ), which obey the dimensionless Boltzmann equation

$$f_i(\vec{x} + \vec{e}_i \Delta t, t + \Delta t) - f_i(\vec{x}, t) = -\frac{\Delta t}{\tau} [f_i(\vec{x}, t) - f_i^{eq}(\vec{x}, t)], \quad (1)$$

in which  $\vec{x}$  and  $t$  are the spatial and time coordinates, respectively;  $[\vec{e}_i]$ , ( $i = 0, \dots, N-1$ ) is the set of  $N$  discrete velocities;  $\Delta t$  is the time step; and  $\tau$  is the relaxation time given by the unique non-null eigenvalue of the collision term in the BGK-approximation. [20] The kinematic viscosity of the flow is strictly related to  $\tau$  as  $\nu = c_s^2 (\tau - \frac{1}{2}) \Delta t$ , being  $c_s = \frac{1}{\sqrt{3}} \frac{\Delta x}{\Delta t}$  the reticular speed of sound. The moments of the distribution functions define the fluid density  $\rho = \sum_i f_i$ , velocity  $\rho \vec{u} = \sum_i f_i \vec{e}_i$ , and pressure  $p = c_s^2 \rho = c_s^2 \sum_i f_i$ . The local equilibrium density functions  $[f_i^{eq}]$  ( $i = 0, \dots, N-1$ ) are expressed by the Maxwell-Boltzmann distribution:

$$f_i^{eq}(\vec{x}, t) = \omega_i \rho \left[ 1 + \frac{1}{c_s^2} (\vec{e}_i \cdot \vec{u}) + \frac{1}{2c_s^4} (\vec{e}_i \cdot \vec{u})^2 - \frac{1}{2c_s^2} (\vec{u} \cdot \vec{u}) \right]. \quad (2)$$

On the two-dimensional square lattice with  $N = 9$  speeds ( $D2Q9$ ) [21], the set of discrete velocities is given by

$$\vec{e}_i = \begin{cases} (0, 0), & \text{if } i = 0 \\ \left( \cos\left(\frac{(i-1)\pi}{2}\right), \sin\left(\frac{(i-1)\pi}{2}\right) \right), & \text{if } i = 1-4 \\ \sqrt{2} \left( \cos\left(\frac{(2i-9)\pi}{4}\right), \sin\left(\frac{(2i-9)\pi}{4}\right) \right), & \text{if } i = 5-8 \end{cases} \quad (3)$$

with the weight,  $\omega_i = 1/9$  for  $i = 1-4$ ,  $\omega_i = 1/36$  for  $i = 5-8$ , and  $\omega_0 = 4/9$ . Here, we adopt a discretization in the velocity space of the equilibrium distribution based on the Hermite polynomial expansion of this distribution [22].

## 2.2. IMMERSED BOUNDARY TREATMENT

Deforming body models are commonly based on continuum approaches using strain energy functions to compute the membrane response. [23–25] However, a particle-based model governed by molecular dynamics has emerged due to its mathematical simplicity while providing consistent predictions. [26, 7, 27, 28] Following this, a particle-based model is here adopted via the Immersed-Boundary (IB) technique. The immersed body consists in a network of  $nv$  vertices linked with  $nl$  linear elements, whose centroids are usually referred as *Lagrangian markers*. An effective forcing term  $[\vec{\mathcal{F}}_i](i = 0, \dots, 8)$ , accounting for the immersed boundary, is included as an additional contribution on the right-hand side of Eq.(1):

$$f_i(\vec{x} + \vec{e}_i \Delta t, t + \Delta t) - f_i(\vec{x}, t) = -\frac{\Delta t}{\tau} [f_i(\vec{x}, t) - f_i^{eq}(\vec{x}, t)] + \Delta t \vec{\mathcal{F}}_i. \quad (4)$$

$\vec{\mathcal{F}}_i$  is expanded in term of the reticular Mach number,  $\frac{\vec{e}_i}{c_s}$ , resulting in:

$$\vec{\mathcal{F}}_i = \left( 1 - \frac{1}{2\tau} \omega_i \left[ \frac{\vec{e}_i - \vec{u}}{c_s^2} + \frac{\vec{e}_i \cdot \vec{u}}{c_s^4} \vec{e}_i \right] \right) \cdot \vec{f}_{ib}, \quad (5)$$

where  $\vec{f}_{ib}$  is a body force term. Due to the presence of the forcing term, the momentum density are derived as  $\rho \vec{u} = \sum_i f_i \vec{e}_i + \frac{\Delta t}{2} \vec{\mathcal{F}}_i$ .

Notably, in such a framework, the forced Navier–Stokes equations can be recovered with a second order accuracy. [29–33]  $\vec{\mathcal{F}}_i$  accounts for the presence of an arbitrary shaped body immersed into the flow field, whereas the external boundaries of the computational domain are treated with the Zou and He known velocity bounce back conditions. [34] The Immersed Boundary (IB) procedure, which was extensively proposed and validated by Coclite and collaborators [17, 18, 35, 15, 16], is here adopted and the moving-least squares reconstruction by Vanella et al. [36] is employed to exchange all Lattice Boltzmann (LB) distribution functions between the Eulerian lattice and the Lagrangian chain, while the body force term in Eq.(5),  $\vec{f}_{ib}$ , is evaluated

through the formulation by Favier et al. [37].

**Elastic Membrane Deformation.** Membranes are subject to elastic strain response, bending resistance, and total enclosed area conservation. The stretching elastic potential acting on the two vertices sharing the  $l$ -th element is given as

$$V_l^s = \frac{1}{2}k_s(l_l - l_{l,0})^2, \quad (6)$$

being  $k_s$  the elastic constant,  $l_l$  the current length of the  $l$ -th element, and  $l_{l,0}$  the length of the  $l$ -th element in the stress-free configuration. Differentiating of the potential energy with respect to the displacements, the nodal forces corresponding to the elastic energy for nodes 1 and 2 connected by edge  $l$  reads as

$$\begin{cases} \vec{F}_1^s = -k_s(l - l_0) \frac{\vec{r}_{1,2}}{l}, \\ \vec{F}_2^s = -k_s(l - l_0) \frac{\vec{r}_{2,1}}{l}, \end{cases} \quad (7)$$

where  $\vec{r}_{i,j} = \vec{r}_i - \vec{r}_j$  and  $r_i$  is the position vector of the node  $i$ .

The bending resistance related to the  $v$ -th vertex connecting two adjacent element is

$$V_v^b = \frac{1}{2}k_b(k_v - k_{v,0})^2, \quad (8)$$

with  $k_b$  the characteristics bending constant,  $k_v$  the current local curvature in the  $v$ -th vertex;  $k_{v,0}$  the local curvature in the  $v$ -th vertex for the stress-free configuration which is evaluated by measuring the variation of the angle between the two adjacent elements  $(\theta - \theta_0)$ , with  $\theta_0$  the angle in the stress free configuration. The forces on the nodes  $v_{left}$ ,  $v$ , and  $v_{right}$  are obtained considering the

relation between the local curvature and the angle as

$$\begin{cases} \vec{F}_{v_{left}}^b = k_b(\theta - \theta_0) \frac{l_{left}}{l_{left} + l_{right}} \vec{n}_v, \\ \vec{F}_v^b = -k_b(\theta - \theta_0) \vec{n}_v, \\ \vec{F}_{v_{right}}^b = k_b(\theta - \theta_0) \frac{l_{right}}{l_{left} + l_{right}} \vec{n}_v, \end{cases} \quad (9)$$

where  $l_{right}$  and  $l_{left}$  are the length of the two adjacent left and right edges, respectively, and  $\vec{n}_v$  is the outward unity vector centered in  $v$ . In this simplified model for the description of the bending resistance the relation between the strain response constant  $k_s$  and  $k_b$  is expressed through  $E_b = \frac{k_b}{k_s r^2}$ , where  $r$  is the particle radius.

In order to limit the membrane stretching, an effective pressure force term is considered. Thus, the penalty force is expressed in term of the reference pressure  $p_{ref}$  and directed along the normal inward unity vector of the  $l$ -th element  $(\vec{n}_l)^-$ , as

$$\vec{F}_l^a = -k_a \left(1 - \frac{A}{A_0}\right) p_{ref} (\vec{n}_l)^- l_l, \quad (10)$$

with  $l_l$  the length of the selected element,  $k_a$  the incompressibility coefficient,  $A$  the current enclosed area,  $A_0$  the enclosed area in the stress-free configuration. [The enclosed area is computed using the Green's theorem along the curve  \$A = \frac{1}{2} \sum\_l x\_l dy\_l\$ .](#) Within this formulation  $k_a = 1$  returns a perfectly incompressible membrane. Note that  $\vec{F}_l^a$  is evenly distributed to the two vertices connecting the  $l$ -th element ( $v_{left}$  and  $v_{right}$ ) as  $\vec{F}_l^a = 0.5 \vec{F}_{v_{left}}^a + 0.5 \vec{F}_{v_{right}}^a$ .

**Particle-Particle Interaction** Two-body interactions are modeled through a repulsive potential centered in each vertex composing the immersed particles. The repulsive force is such that the minimum allowed distance between two vertices coming from two different particles is  $\Delta x$ . The impulse acting on vertex 1, at a distance  $d_{1,2}$  from the vertex 2 of an adjacent particle, is directed

in the inward normal direction identified by  $(\vec{n}_1)^-$  and is given by:

$$\vec{F}_1^{pp} = \frac{10^{-4}}{8\sqrt{2}} \sqrt{\frac{\Delta x}{d_{1,2}^5}} (\vec{n}_1)^-. \quad (11)$$

**Wall-Particle Interaction** With no intent of being exhaustive, a wide range of vascular molecules are involved in the adhesion process, including E- and P-selectins,  $\alpha_v\beta_3$  and  $\alpha_v\beta_5$  integrins, VCAM-1 and ICAM-1 adhesion molecules. [38–40] In the present work, the author only consider the effect of ICAM-like adhesion molecules, meaning a short-range ligand-receptor interaction. Ligand molecules are distributed over the surfaces of the particle with density  $\rho_l$ ; while receptor molecules are uniformly distributed over blood vessel walls. [18, 41] Ligand molecules are modeled as linear springs, which tend to establish bonds with receptors on the vascular wall, resulting in a mechanical force given as

$$\vec{F}_l^{wp} = \sigma(y_l - y_{cr,eq})\vec{n}_l, \quad (12)$$

where  $y_l$  is the bond length,  $y_{cr,eq}$  the equilibrium bond length and  $\sigma$  the spring constant (same for all springs). Bonds can be generated only if the minimum separation distance between the particle boundary and the wall is smaller than a critical value,  $y_{cr} = 25\text{ nm}$  [42] whereas the equilibrium bond length, resulting in a null force, is  $y_{cr,eq} = 0.5y_{cr}$ . The linear spring constant is computed in *lattice units* through its dimensionless group,  $\frac{\rho_{ref} v_{ref}^2}{H}$ , where  $\rho_{ref}$ ,  $H$ , and  $v_{ref}$  are the reference density, length, and viscosity, respectively. The spring constant  $\sigma$  ranges from 0.5 to 2.0. These values return a plausible agreement with experimental observations and were validated against experimental data in two previous work by the author and collaborators [18, 35]. At each time step, the bond formation is regulated by a forward probability function, while a reverse probability function controls the destruction of a pre-existing bond, see for details [18]. The adhesive force, being calculated at the centroid of each element, is evenly distributed to the two vertices connecting the element in the same fashion used for  $\vec{F}^a$ .



**Hydrodynamics Stresses** Pressure and viscous stresses exerted by the  $l$ -th linear element are:

$$\vec{F}_l^p(t) = (-p_l \vec{n}_l) l_l, \quad (13)$$

$$\vec{F}_l^\tau(t) = (\bar{\tau}_l \cdot \vec{n}_l) l_l, \quad (14)$$

where  $\bar{\tau}_l$  and  $p_l$  are the viscous stress tensor and the pressure evaluated in the centroid of the element, respectively;  $\vec{n}_l$  is the outward normal unit vector while  $l_l$  is its length. The pressure and velocity derivatives in Eq.s (13) and (14) are evaluated considering a probe in the normal positive direction of each element, being the probe length  $1.2 \Delta x$ , and using the cited moving least squares formulation [36]. In this framework, the velocity derivatives evaluated at the probe are considered equal to the ones on the linear element centroid and all force contributions are computed with respect to the centroid of each elements and then transferred to the vertices. [43]

### 2.3. FLUID-STRUCTURE INTERACTION

The motion of the immersed bodies is described differently for red cells and particles, for saving computational costs.

On one side, blood cells are transported using the *kinematic IB* technique described in [16], so that advecting the velocity of the Lagrangian points with the underlying Eulerian fluid velocity and then applying internal stresses, Eq.s (7), (9), (10), and (11) through the volume force in the flow equations to include the body effect on the flow field Eq.(5). *On one side, blood cells are transported using the kinematic IB technique described in [16]; so that, advecting the velocity of the Lagrangian points with the underlying Eulerian fluid velocity and then applying internal stresses (Eq.s (7), (9), (10), and (11)) through the volume force in the flow equations using Eq.(5).* On the other side, the particles dynamics is determined by *dynamics IB* technique described in [16], using the solution of the Newton equation for each Lagrangian vertex, accounting for both internal, Eq.s (7), (9), (10), (11), and (12) and external stresses, Eq.s (13) and (14). Thus, no-slip

boundary conditions are imposed using a weak coupling approach. [17]

**Blood Cells Motion.** The position of the  $v$ -th vertex is updated at each time step considering the vertices moving with the velocity of the withstanding fluid. For each vertex nine Eulerian points are considered, namely the Eulerian points falling into the two-dimensional support domain, defined as a square with side equal  $2.6\Delta x$  and the velocity of each Lagrangian point,  $\dot{\vec{x}}(t)$ , is computed interpolating the velocity of the fluid in the nine associated Eulerian points. Finally, the position of each Lagrangian point is computed as:

$$\vec{x}(t) = \frac{2}{3}(2\vec{x}(t - \Delta t) - \frac{1}{2}\vec{x}(t - 2\Delta t) + \dot{\vec{x}}(t)\Delta t). \quad (15)$$

**Elastic Particles Motion.** The total force  $\vec{F}_v^{tot}(t)$  acting on the  $v$ -th element of the immersed body is evaluated in time and the position of the vertices is updated at each Newtonian dynamics time step considering the membrane mass uniformly distributed over the  $m_v$  vertices,

$$m_v \dot{\vec{u}}_v = \vec{F}_v^{tot}(t) = \vec{F}_v^s(t) + \vec{F}_v^b(t) + \vec{F}_v^a(t) + \vec{F}_v^{pp}(t) + \vec{F}_v^{wp}(t) + \vec{F}_v^p(t) + \vec{F}_v^\tau(t). \quad (16)$$

The Verlet algorithm is employed to integrate the Newton equation of motion. Precisely, a first tentative velocity is considered into the integration process,  $\dot{\vec{x}}_{v,0}(t)$ , obtained interpolating the fluid velocity from the surrounding lattice nodes

$$\vec{x}_v(t + \Delta t) = \vec{x}_v(t) + \dot{\vec{x}}_{v,0}(t)\Delta t + \frac{1}{2} \frac{\vec{F}_v^{tot}(t)}{m_v} \Delta t^2 + O(\Delta t^3), \quad (17)$$

then, the velocity at the time level  $t + \Delta t$  is computed as

$$\vec{u}_v(t + \Delta t) = \frac{\frac{3}{2}\vec{x}_v(t + \Delta t) - 2\vec{x}_v(t) + \frac{1}{2}\vec{x}_v(t - \Delta t)}{\Delta t} + O(\Delta t^2). \quad (18)$$

**Rigid Particles Motion.** Rigid motion is readily obtained integrating all stresses contributions

over the particles boundary and updating both, linear and angular velocity in time as  $\vec{u}(t) = \frac{\vec{F}^{tot}(t)}{m}$  and  $\dot{\omega}(t) = \frac{M^{tot}(t)}{I}$ . Here  $m$  is the particle mass,  $\vec{F}^{tot}(t)$  is the total force exerted by the particle;  $M^{tot}(t)$  is the total moment acting on the particle, and  $I$  is the moment of inertia. Finally,  $\vec{u}(t)$  and  $\omega(t)$  are computed as

$$\vec{u}(t) = \frac{2}{3}(2\vec{u}(t - \Delta t) - \frac{1}{2}\vec{u}(t - 2\Delta t) + \dot{\vec{u}}(t)\Delta t) + O(\Delta t^2), \quad (19)$$

$$\omega(t) = \frac{2}{3}(2\omega(t - \Delta t) - \frac{1}{2}\omega(t - 2\Delta t) + \dot{\omega}(t)\Delta t) + O(\Delta t^2), \quad (20)$$

with  $\Delta x = \Delta t = 1$ . The proposed approach is unconditionally stable for small local velocity variations within any solid/fluid density ratio [44], which is indeed the case of the present work.

### 3. RESULTS AND DISCUSSION

#### 3.1. GEOMETRY AND BOUNDARY CONDITIONS OF THE PROBLEM.

To predict the interaction dynamics of particles with red blood cells navigating a capillary (**Figure.1**), the combined Lattice Boltzmann–Immersed Boundary method by Coclite et al. [16] is adopted. The capillary flow is modeled within a rectangular channel with a height of  $H = 10\mu m$  and length  $5H$ , with periodic boundary conditions along  $x$  while on the walls of the channel no-slip conditions are imposed (**Figure.1a**). A plane Hagen-Poiseuille flow is obtained by imposing a linear pressure drop  $\Delta p$  ( $= \frac{8u_{max}^2}{H} \frac{\rho x}{Re}$ ) along the channel as function of the Reynolds number  $Re = \frac{u_{max}H}{\nu} = 10^{-2}$ . The reference kinematic viscosity is chosen as the water kinematic viscosity,  $\nu = 1.2 \times 10^{-6} \text{ m}^2/\text{s}$ , thus resulting in the centerline velocity  $u_{max} = 1.2 \times 10^{-3} \text{ m/s}$ . The channel height is discretized with 200 computational cells, corresponding to  $\Delta x = 50 \text{ nm}$ . Five initial configurations composed by four particles each are placed initially at the rest into the computational domain along with four different initial distributions of red cells (**Figure.1.b**). The portion of fluid enclosed into cell boundaries is about the 20% of the total computational domain. Both, red blood cells and particles are discretized with linear elements to obtain the ratio between solid and fluid

meshes as  $0.3\Delta x$ . The resting configuration of a red blood cell is parametrized as the median section of a three-dimensional red blood cell [45, 46],

$$\begin{cases} x = a\alpha \sin q \\ y = a\frac{\alpha}{2}(0.207 + 2.003\sin^2 q - 1.123\sin^4 q)\cos q \end{cases} \quad (21)$$

where  $a$  is 1.0,  $\alpha$  is the cell radius,  $3.5\mu m$ , and  $q$  varies in  $[-0.5\pi, 1.5\pi]$ . [47] The stiffness of such blood cells is regulated by the capillary number,  $Ca=10^{-2}$  ( $=\rho v u_{\max}/k_s$ ) with null bending resistance,  $Eb = 0$ . The membrane stiffness is assumed as  $k_s = 1.5 \times 10^{-4}$  Nm [48, 49] On the other side, particles are discretized as initially circular membranes with  $Ca=10^{-2}$  and  $Eb = 0.05$  ( $=k_b/k_s r^2$ ), where  $r$  ( $=0.5\mu m$ ) is the particles radius; or transported as rigid objects. The particles surface is decorated by ligand molecules with a density  $\rho_L = 0.5$ . These ligands interact with receptors expressed uniformly on the capillary walls forming ligand-receptor bonds with a biochemical affinity given by  $k_f/k_{r,0} = 8.5 \times 10^3$  and a bond strength of  $\sigma = \frac{\rho_{ref} v_{ref}^2}{H} = 0.5, 1$ , and 2. [50, 51] The density of all particles is slightly higher than that of the surrounding fluid, being  $\frac{\rho_p}{\rho} = 1.1$ . Thermal fluctuations are neglected, here, being almost uninfluential for micrometric and sub-micrometric particles under flow. [52]

### 3.2. FLOW REGIMENS IN $10\mu m$ CAPILLARY

Since the great separation in the occupied fluid area between red blood cells and particles ( $A_{RBC,Tot}/A_{part,Tot} = 34.74$ ), particle-particle collisions are rare events while RBC-particle interactions dominate the redistribution of particles into the flow field. As a consequence, the redistribution of RBCs into the flow field govern the journey of particles in the blood stream. [53, 54] Thus, the transport of red blood cells alone is firstly considered in terms of the overall cell configurations and trajectories (**Figure.2**). The simplest initial configuration possible, depicted in **Figure.1.b**, is a "single-filed" distribution of RBCs. Indeed, the intrinsically equilibrated flow field led the cells to null lateral displacement while reaching the typical parachute shape (**Figure.2.a**). [55] Indeed,

the presence of immersed cells perturb the flow by forming different layers as demonstrated in **Figure.2.a**. The slip velocity field, depicted in **Figure.2.a**, computed as the difference between the velocity field obtained when transporting the cells ( $\frac{u_x}{u_{max}}$ ) and the velocity field with no cells immersed in the fluid ( $\frac{u_{x,NoC}}{u_{max}}$ ), clearly shows the effect of the presence of elastic membranes into the flow. Precisely, the membranes response to the exerted hydrodynamics forces is wide and negative into the higher fluid laminae, localized and positive at the cells peripheries (see **Figure.2.a**). Interestingly, the formation of such layers is strongly emphasized when considering the out of plane vorticity patterns reported in **Figure.2.b**. Here, the higher velocity fluid laminae are characterized by almost null vorticity values; on the contrary, cell extrema present the highest values. Thus, one can identify three fluid regions: a bulk zone, RBC-rich zone ( $4 \mu m$ ) in which the flow is strongly affected by the presence of large cells immersed in,  $0.3 \leq y/H \leq 0.7$ ; an intermediate zone,  $1.0 \mu m$  high layer, in which the flow is slightly perturbed by the presence of cells peripheries,  $0.2 < y/H < 0.3$  and  $0.7 < y/H < 0.8$ ; and the cell-free layer, region of essentially undisturbed flow,  $0 < y/H < 0.2$  and  $0.8 < y/H < 1$ . Commonly, the cell-free layer and the intermediate zone are considered as a single fluid lamina by the height of  $3 \mu m$  for a capillary flow at  $Re = 0.01$  in a  $10 \mu m$  vessel with 20% hematocrit while for the scope of the present work the two flow regions are considered separately. [56, 57]

With the idea of shuffling the RBCs initial conditions, three different disordered initial configurations are computed in addition, see **Figure.1.b**. Large cells tend to occupy higher velocity regions regardless to their releasing lateral position as demonstrated by observing the cells trajectories (**Figure.2.c**, **2.d**, and **2.e**). Immersed membranes tend to equilibrate the velocity and pressure fields across their boundary; being the plane Hagen-Poiseuille flow symmetric with respect to the centerline, large cells tend to move across flow streamlines in order to have their upper and lower hemi-surfaces equally distributed below and above the centerline. This phenomenon is strongly empathized by the size of these membranes because of the large difference in the dragging fluid velocity across their boundaries. [47]

### 3.3. MICROCONSTRUCT MARGINATION AS A FUNCTION OF RED BLOOD CELL DISTRIBUTION.

The vascular journey of rigid and soft particles is now considered in terms of their trajectories and measuring the number of particles populating the three identified fluid regions. Firstly, the five different configurations of rigid ( $Ca = 0$ ) and soft ( $Ca = 10^{-2}$ ) particles are transported one per time within the "single-filed" RBC distribution as depicted in **Figure.1.b**. All particles (regardless from their rigidity) tend to avoid direct bumps with RBCs and accommodate themselves outside the perturbed flow regions; specifically, or between two RBCs or outside the bulk zone as demonstrated in **Figure.3.b** and **Figure.3.c** for  $Ca = 0$  and  $Ca = 10^{-2}$ , respectively. Quantitatively, about 50% of the particles are initially released into the bulk zone along with 40% into the cell-free layer and 10% in the intermediate zone; then, after  $6tu_{\max}/H$  the number of rigid particles in the margination layer increases by 20%, the intermediate zone becomes completely unpopulated and the bulk loses about 10% of particles (**Figure.3.d**). Analogous trends are found when transporting the five different particle configurations with  $Ca = 10^{-2}$  (**Figure.3.e**).

On the other hand, when the particles are transported into disordered RBC distributions, the interactions between particles and cells become more relevant and slight changes in the RBC releasing positions strongly affect particle trajectories. In fact, rigid particles' trajectories present discontinuities due to elastic bumps with RBCs because of their impossibility to adsorb the exchanged momentum (top insets in **Figure.4.a**, **.4.c**, and **.4.e**); on the contrary, the elastic capabilities of soft particles give smoother trajectories and the number of contacts with cells (discontinuities in the trajectories) is dramatically limited (top insets in **Figure.4.b**, **.4.d**, and **.4.f**). Interestingly, switching to a disordered initial RBC configuration poorly affects the measured final number of particles populating the three identified flow regions with respect to the single-filed RBC positioning regardless of their stiffness. Nonetheless, disordered red blood cell initial conditions return different functional behavior for the particles distributions due to the increased number of RBC-particle interactions. Indeed, straightforward cell dynamics led to almost monotonic variations of the number of particle in the three regions while complex cell dynamics led to non-smooth distributions. Note

that, the idealized configurations of the computational domain (straight rectangular channel with periodic boundary conditions) neglect the recombination effect of the RBC distributions caused by enlargements or restrictions into blood vessels. This recombination effect may play a major role in the margination mechanics, continuously shuffling the red blood cell distributions in the vasculature.

### 3.4. ADHESION MECHANICS OF PARTICLES IN NARROW CAPILLARIES.

Particles sufficiently near endothelial walls are captured by the ligand-receptor mediated interaction presented in the **Computational Method** section. Before drawing the quantitative collective behavior of particles as a function of their stiffness, we focus on the adhesion mechanics of representative rigid and soft particles in the cell-free layer (CFL) for three different values of the bond strength,  $\sigma = 0.5, 1$ , and  $2$ . The flow into the CFL is assimilated to a planar Couette flow at  $Re = 0.003$  ( $= \frac{H_{CFL} u_{max}}{\nu}$ ), with  $H_{CFL} = 3\mu m$ . The computational domain is a rectangle in which the height is discretized with  $H_{CFL} = 200\Delta x$  with  $\Delta x = 15nm$  and length correspond to  $3H_{CFL}$  with periodic boundary conditions along  $x$ .

Rigid particles preferentially roll over the endothelial wall with their motility restrained proportionally to  $\sigma$  (left insets in **Figure.5.a**, **Figure.5.b**, and **Figure.5.c**). On the other hand, soft membranes may be or dislodged away from the vasculature (right inset in **Figure.5.a**); or roll on the endothelium continuously forming and destroying chemical bonds (right inset in **Figure.5.b**); or firmly adhering the vasculature deforming to maximize the contact surface (right inset in **Figure.5.c**). This dynamics is quantified *via* rolling velocity measurement of such particles (see **Figure.5.d**). For  $\sigma = 0.5$  the rigid particle interacts with the wall rolling with  $\frac{u_{roll}}{u_{max}} = 0.153 \pm 0.02$ . Then, increasing the bond strength the rolling velocity is restrained to  $\frac{u_{roll}}{u_{max}} = 0.140 \pm 0.09$  for  $\sigma = 1.0$  and  $\frac{u_{roll}}{u_{max}} = 0.08 \pm 0.25$  for  $\sigma = 2.0$ . On the other side, the soft particle with  $\sigma = 0.5$  weakly interacts with the endothelium until  $\frac{t u_{max}}{H_{CFL}} = 2.3$  then detaches and moves towards higher velocity streamlines; for  $\sigma = 1.0$  the particle stably rolls with  $\frac{u_{roll}}{u_{max}} = 0.142 \pm 0.01$ ; and for  $\sigma = 2.0$  their velocity oscillate around zero,  $\frac{u_{roll}}{u_{max}} = 0.0 \pm 0.05$  after a short transitory period (right inset in

**Figure.5.d).** The adhesion mechanics of such particles is further characterized by computing the number of closed chemical bonds in time with respect to the number of bonds originally closed in the initial configuration,  $n_L/n_{L,0}$  (**Figure.5.f**). Indeed, rigid particles establish about the same number of bonds ( $\frac{n_L}{n_{L,0}} = 1.21$ ) regardless from  $\sigma$ . By varying the contact region, soft particles may vary the number of closed bonds from zero for  $\sigma = 0.5$  to  $\frac{n_L}{n_{L,0}} = 1.5$  and  $\frac{n_L}{n_{L,0}} = 4.6$  for  $\sigma = 1.0$  and  $2.0$ , respectively, thus establishing firm adhesion with the vascular walls.

### 3.5. PARTICLE REGIMENS IN 10 $\mu m$ HIGH BLOOD CAPILLARY.

Here, a thorough characterization of particle margination and adhesion abilities is given in terms of local and averaged quantities within the four RBC configurations. Firstly, the final lateral positions of all particles is drawn against their releasing positions in **Figure.6.a** and **.6.b**, for rigid and soft particles, respectively. If no cells traversed the capillary, due to the small Reynolds number and the small particle dimensions, almost null lateral displacements would be observed and the distribution of  $y_{fin}/H$  would overlap the bisector of the plotted plane. On the contrary, due to the presence of cells, these points form a cloud around the bisector. In particular, regardless from the particles' stiffness, small displacements are measured when transporting particles in the 1<sup>st</sup> RBC configuration (black dots in **Figure.6.a** and **Figure.6.b**) while for the other three configurations the largest lateral displacements are observed for particles released into the bulk zone  $0.3 \leq y_0/H \leq 0.7$  (symbols in **Figure.6.a** and **.6.b**). The maximum radial displacement observed in the computations, averaged over all transported particles in the four RBC configurations is drawn in **Figure.6.c** as a function of the flow region in which particles are initially set. Interestingly, the two particle families behave differently when released into the intermediate zone and in the cell-free layer. In fact, when released into the intermediate zone, rigid particle exert, at the most a lateral dislodging of  $\frac{\langle r_{max} \rangle}{H} = 0.147 \pm 0.052$ , while for soft particle  $\frac{\langle r_{max} \rangle}{H} = 0.115 \pm 0.017$  (green bars in **Figure.6.c**). Then, rigid particles released into the cell-free layer move up to  $\frac{\langle r_{max} \rangle}{H} = 0.050 \pm 0.0047$  while soft particles move toward the centerline by about  $\frac{\langle r_{max} \rangle}{H} = 0.095 \pm 0.0056$  (orange bars in **Figure.6.c**). These small but statistically significant dif-



ferences are due to the role of the stiffness, as already underlined in the previous sections; rigid particles are strongly scattered by RBCs while soft particles are dislodged away gently from the blood cell bulk. On the other side, rigid particles, if released into the cell-free layer, tend to avoid any direct bump with RBCs and to not move into any fluid regions perturbed by the presence of cells. The average lateral velocity measured in the computations for rigid and soft particles is drawn in **Figure.6.d** and confirms the trends depicted. The average number of particles populating the three discussed flow regions in time demonstrate that regardless from their rigidity the particles would tend to migrate out of the intermediate zone and marginate with about the same ratio (**Figure.6.e**). Lastly, over the total number of particles found at  $\frac{tu_{max}}{H} = 10$  in the cell-free layer, the number of particles interacting with the endothelium is about 26% for rigid constructs and 24% for soft membranes. Only the 6% of the rigid particles can firmly adhere the vasculature *versus* the 23% of the soft particles (**Figure.6.f**).

The depicted complex mechanics explains the rationale behind the choice of soft nanomedicines over their rigid counterpart. In this specific cases, the margination ability of particles seems not depend on their stiffness while their adhesive abilities are dramatically influenced by the rigidity. These trends are, in turn, confirmed by experimental findings of M. B. Fish and colleagues [58]. They measured the accumulation of rigid and soft particles on vasculature walls for different flow rates and particle sizes concluding that soft particles are preferable for low shear rates while rigid constructs for high-speed flows. Note that, in this context, the overall accumulation of vascular targeted drug carriers depends on their margination and adhesion abilities at the same time.

## CONCLUSIONS

A combined Lattice Boltzmann - Immersed Boundary Method is employed to predict the margination and adhesive abilities of micrometric circular particles in narrow capillaries in presence of whole blood with 20% hematocrit. Specifically, these abilities are systematically assessed by transporting five independent configuration of four rigid ( $Ca = 0$ ) and soft ( $Ca = 10^{-2}$ ) par-

ticles each, one per time, within four different red blood cell distributions (one single-filed and three non-filed disordered configurations). The perimeter of these particle is decorated with ligands molecules (with density  $\rho_L = 0.5$ ) that may interact with receptors molecules laying on the endothelial walls. Moreover, the analysis of the adhesion mechanics of such micrometric circular constructs is carried out on a finer mesh ( $\Delta x = 15\text{ nm}$ ) by transporting them with different ligand-receptor bond strength ( $\sigma = 0.5, 1.0, \text{ and } 2.0$ ) in a planar linear flow imitating the flow in the cell-free layer.

Firstly, it is measured the formation of three different fluid regions where only blood cells are transported, namely, the bulk, the intermediate zone and the cell-free layer. Then, the vascular journey of soft and rigid particles is analyzed in terms of their trajectories and their accumulation in these three identified regions, thus observing that rigid particles tend to marginate in the same fashion than their soft counterpart even if, neglecting the rigidity, the number of elastic bumps with blood cells dramatically decreases. Nonetheless, soft particles can adhere to the vasculature more efficiently than their rigid counterpart. In fact, only 6% of the total number of rigid particles can firmly adhere to the vasculature while this number grows up to 23% when considering soft membranes.

Collectively, these data continue to demonstrate the abilities of soft nanomedicines for the precise and specific delivery of therapeutics. Particularly, in narrow capillaries particle stiffness does not affect the margination rate. On the contrary, particle stiffness strongly affects the ability to efficiently interact with the endothelium and firmly adhere to the walls. *Indeed, soft and rigid particles would behave differently for larger Reynolds number. For example, it has been proven that, depending on the peculiar shape, particles tend to marginate faster for  $\text{Re} > 100$  and may stop their rotative motion around their axis. Moreover, particles adhesion would be largely influenced by stronger hydrodynamics forces. However, these phenomena are far from the present work scope and will be object of future investigations.*

## ACKNOWLEDGMENTS

The author acknowledge Dr. P. Decuzzi for the fruitful discussions about margination phenomenology; Prof. G. Pascazio and Prof. M. D. de Tullio for the deep knowledge shared onto the numerical modeling of IBM and for providing CPU hours.

## REFERENCES

### References

- [1] D. Peer, J. Karp, S. Hong, O.C. Farokhzad, R. Margalit, and R. Langer. Nanocarriers as an emerging platform for cancer therapy. Nature nanotechnology, 2:751–60, 2007.
- [2] Charalambos Antoniadis, Costantinos Psarros, Dimitris Tousoulis, Constantinos Bakogiannis, Cheerag Shirodaria, and Christodoulos Stefanadis. Nanoparticles: a promising therapeutic approach in atherosclerosis. Current drug delivery, 7(4):303–311, 2010.
- [3] P Decuzzi, B Godin, T Tanaka, S-Y Lee, C Chiappini, X Liu, and M Ferrari. Size and shape effects in the biodistribution of intravascularly injected particles. Journal of Controlled Release, 141(3):320–327, 2010.
- [4] Paolo Decuzzi. Facilitating the clinical integration of nanomedicines: the roles of theoretical and computational scientists. ACS nano, 10(9):8133–8138, 2016.
- [5] K. Muller, D.A. Fedosov, and G. Gompper. Margination of micro- and nano-particles in blood flow and its effect on drug delivery. Scientific Reports, 4, 2014. doi: 10.1038/srep04871.
- [6] D.A. Fedosov, W. Pan, B. Caswell, G. Gompper, and G.E. Karniadakis. Predicting human blood viscosity in silico. Proceedings of the National Academy of Sciences of the United States of America, 108(29):11772–11777, 2011. doi: 10.1073/pnas.1101210108.
- [7] Dmitry A Fedosov, Huan Lei, Bruce Caswell, Subra Suresh, and George E Karniadakis. Multiscale modeling of red blood cell mechanics and blood flow in malaria. PLoS computational biology, 7(12):e1002270, 2011.
- [8] Simone Melchionna. A model for red blood cells in simulations of large-scale blood flows. Macromolecular Theory and Simulations, 20(7):548–561, 2011.
- [9] Lampros Mountrakis, Eric Lorenz, and Alfons G Hoekstra. Validation of an efficient two-dimensional model for dense suspensions of red blood cells. International Journal of Modern Physics C, 25(12):1441005, 2014.
- [10] Andrew P Spann, James E Campbell, Sean R Fitzgibbon, Armando Rodriguez, Andrew P Cap, Lorne H Blackburn, and Eric SG Shaqfeh. The effect of hematocrit on platelet adhesion: experiments and simulations. Biophysical journal, 111(3):577–588, 2016.

- [11] Daniel A Reasor, Marmar Mehrabadi, David N Ku, and Cyrus K Aidun. Determination of critical parameters in platelet margination. Annals of biomedical engineering, 41(2):238–249, 2013.
- [12] Amit Kumar and Michael D Graham. Margination and segregation in confined flows of blood and other multi-component suspensions. Soft Matter, 8(41):10536–10548, 2012.
- [13] Aaron C. Anselmo, Mengwen Zhang, Sunny Kumar, Douglas R. Vogus, Stefano Menegatti, Matthew E. Helgeson, and Samir Mitragotri. Elasticity of nanoparticles influences their blood circulation, phagocytosis, endocytosis, and targeting. ACS Nano, 9(3):3169–3177, 2015. doi: 10.1021/acsnano.5b00147.
- [14] L Mountrakis, E Lorenz, and AG Hoekstra. Where do the platelets go? a simulation study of fully resolved blood flow through aneurysmal vessels. Interface Focus, 3(2):20120089, 2013.
- [15] A. Coclite, G. Pascasio, M.D. de Tullio, and P. Decuzzi. Predicting the vascular adhesion of deformable drug carriers in narrow capillaries traversed by blood cells. Journal of Fluids and Structures, 82:638 – 650, 2018. ISSN 0889-9746. doi: <https://doi.org/10.1016/j.jfluidstructs.2018.08.001>. URL <http://www.sciencedirect.com/science/article/pii/S0889974618301944>.
- [16] A. Coclite, S. Ranaldo, M.D. de Tullio, P. Decuzzi, and G. Pascasio. Kinematic and dynamic forcing strategies for predicting the transport of inertial capsules via a combined lattice boltzmann immersed boundary method. Computers & Fluids, 180:41–53, 2019. ISSN 0045-7930. doi: <https://doi.org/10.1016/j.compfluid.2018.12.014>. URL <http://www.sciencedirect.com/science/article/pii/S0045793018304304>.
- [17] A. Coclite, M. D. de Tullio, G. Pascasio, and P. Decuzzi. A combined lattice boltzmann and immersed boundary approach for predicting the vascular transport of differently shaped particles. Computers & Fluids, 136:260 – 271, 2016. ISSN 0045-7930. doi: <http://dx.doi.org/10.1016/j.compfluid.2016.06.014>.
- [18] A. Coclite, H. Mollica, S. Ranaldo, G. Pascasio, M. D. de Tullio, and P. Decuzzi. Predicting different adhesive regimens of circulating particles at blood capillary walls. Microfluidics and Nanofluidics, 21(11):168, 2017. ISSN 1613-4990. doi: 10.1007/s10404-017-2003-7. URL <https://doi.org/10.1007/s10404-017-2003-7>.
- [19] J. Key, A.L. Palange, F. Gentile, S. Aryal, C. Stigliano, D. Di Mascolo, E. De Rosa, M. Cho, Y. Lee, J. Singh, and P. Decuzzi. Soft discoidal polymeric nanoconstructs resist macrophage uptake and enhance vascular targeting in tumors. ACS Nano, 216:47–55, 2015. doi: 10.1016/j.jconrel.2015.08.015.
- [20] P. L. Bhatnagar, E. P. Gross, and M. Krook. A model for collision processes in gases. i. small amplitude processes in charged and neutral one-component systems. Phys. Rev., 94:511–525, May 1954. doi: 10.1103/PhysRev.94.511.
- [21] Y. H. Qian, D. D’Humières, and P. Lallemand. Lattice bgk models for navier-stokes equation. EPL (Europhysics

- Letters), 17(6):479, 1992.
- [22] Xiaowen Shan, Xue-Feng Yuan, and Hudong Chen. Kinetic theory representation of hydrodynamics: a way beyond the navierstokes equation. Journal of Fluid Mechanics, 550:413–441, 3 2006. ISSN 1469-7645. doi: 10.1017/S0022112005008153.
  - [23] C Pozrikidis. Effect of membrane bending stiffness on the deformation of capsules in simple shear flow. Journal of Fluid Mechanics, 440:269–291, 2001.
  - [24] R Skalak, A Tozeren, RP Zarda, and S Chien. Strain energy function of red blood cell membranes. Biophysical Journal, 13(3):245–264, 1973.
  - [25] Heinrich Krüger. Computer simulation study of collective phenomena in dense suspensions of red blood cells under shear. Springer Science & Business Media, 2012.
  - [26] M Dao, J Li, and S Suresh. Molecularly based analysis of deformation of spectrin network and human erythrocyte. Materials Science and Engineering: C, 26(8):1232–1244, 2006.
  - [27] Masanori Nakamura, Sadao Bessho, and Shigeo Wada. Spring-network-based model of a red blood cell for simulating mesoscopic blood flow. International journal for numerical methods in biomedical engineering, 29(1):114–128, 2013.
  - [28] Swe Soe Ye, Yan Cheng Ng, Justin Tan, Hwa Liang Leo, and Sangho Kim. Two-dimensional strain-hardening membrane model for large deformation behavior of multiple red blood cells in high shear conditions. Theoretical Biology and Medical Modelling, 11(1):19, 2014.
  - [29] Zhaoli Guo, Chuguang Zheng, and Baochang Shi. Force imbalance in lattice boltzmann equation for two-phase flows. Phys. Rev. E, 83:036707, Mar 2011. doi: 10.1103/PhysRevE.83.036707.
  - [30] Alessandro De Rosis, Stefano Ubertini, and Francesco Ubertini. A comparison between the interpolated bounce-back scheme and the immersed boundary method to treat solid boundary conditions for laminar flows in the lattice boltzmann framework. Journal of Scientific Computing, 61(3):477–489, 2014. ISSN 1573-7691. doi: 10.1007/s10915-014-9834-0. URL <http://dx.doi.org/10.1007/s10915-014-9834-0>.
  - [31] Alessandro De Rosis, Stefano Ubertini, and Francesco Ubertini. A partitioned approach for two-dimensional fluid-structure interaction problems by a coupled lattice boltzmann-finite element method with immersed boundary. Journal of Fluids and Structures, 45:202 – 215, 2014. ISSN 0889-9746. doi: <http://dx.doi.org/10.1016/j.jfluidstructs.2013.12.009>.
  - [32] K. Suzuki, K. Minami, and T. Inamuro. Lift and thrust generation by a butterfly-like flapping wing-body model: Immersed boundary-lattice boltzmann simulations. Journal of Fluid Mechanics, 767:659–695, 2015. doi: 10.1017/jfm.2015.57.

- [33] Y. Wang, C. Shu, C.J. Teo, and J. Wu. An immersed boundary-lattice boltzmann flux solver and its applications to fluid-structure interaction problems. Journal of Fluids and Structures, 54:440 – 465, 2015. ISSN 0889-9746. doi: <http://dx.doi.org/10.1016/j.jfluidstructs.2014.12.003>.
- [34] Qisu Zou and Xiaoyi He. On pressure and velocity boundary conditions for the lattice boltzmann bgk model. Physics of Fluids, 9(6):1591–1598, 1997. doi: <http://dx.doi.org/10.1063/1.869307>.
- [35] Hilaria Mollica, Alessandro Coclite, Marco E. Miali, Rui C. Pereira, Laura Paleari, Chiara Manneschi, Andrea DeCensi, and Paolo Decuzzi. Deciphering the relative contribution of vascular inflammation and blood rheology in metastatic spreading. Biomicrofluidics, 12(4):042205, 2018. doi: 10.1063/1.5022879. URL <https://doi.org/10.1063/1.5022879>.
- [36] Marcos Vanella and Elias Balaras. A moving-least-squares reconstruction for embedded-boundary formulations. Journal of Computational Physics, 228(18):6617 – 6628, 2009. ISSN 0021-9991. doi: <http://dx.doi.org/10.1016/j.jcp.2009.06.003>.
- [37] J. Favier, A. Revell, and A. Pinelli. A lattice boltzmann-immersed boundary method to simulate the fluid interaction with moving and slender flexible objects. Journal of Computational Physics, 261:145–161, 2014. doi: 10.1016/j.jcp.2013.12.052.
- [38] Monica M Burdick, J Michael McCaffery, Young S Kim, Bruce S Bochner, and Konstantinos Konstantopoulos. Colon carcinoma cell glycolipids, integrins, and other glycoproteins mediate adhesion to huvecs under flow. American journal of physiology-Cell physiology, 284(4):C977–C987, 2003.
- [39] Steven R Barthel, Jaclyn D Gavino, Leyla Descheny, and Charles J Dimitroff. Targeting selectins and selectin ligands in inflammation and cancer. Expert opinion on therapeutic targets, 11(11):1473–1491, 2007.
- [40] Ja Hye Myung, Khyati A Gajjar, Ryan M Pearson, Cari A Launier, David T Eddington, and Seungpyo Hong. Direct measurements on cd24-mediated rolling of human breast cancer mcf-7 cells on e-selectin. Analytical chemistry, 83(3):1078–1083, 2011.
- [41] Chenghai Sun, Cristiano Migliorini, and Lance L Munn. Red blood cells initiate leukocyte rolling in postcapillary expansions: a lattice boltzmann analysis. Biophysical Journal, 85(1):208–222, 2003.
- [42] Sitikantha Roy and H Jerry Qi. A computational biomimetic study of cell crawling. Biomechanics and modeling in mechanobiology, 9(5):573–581, 2010.
- [43] M. D. de Tullio and G. Pascasio. A moving-least-squares immersed boundary method for simulating the fluid-structure interaction of elastic bodies with arbitrary thickness. Journal of Computational Physics, submitted, 2016.
- [44] Q. Zhang and T. Hisada. Studies of the strong coupling and weak coupling methods in fsi analysis. International

- Journal for Numerical Methods in Engineering, 60(12):2013–2029, 2004. doi: 10.1002/nme.1034.
- [45] C Pozrikidis. Numerical simulation of the flow-induced deformation of red blood cells. Annals of biomedical engineering, 31(10):1194–1205, 2003.
  - [46] Y Sui, YT Chew, P Roy, XB Chen, and HT Low. Transient deformation of elastic capsules in shear flow: effect of membrane bending stiffness. Physical Review E, 75(6):066301, 2007.
  - [47] Lingling Shi, Tsorng-Whay Pan, and Roland Glowinski. Deformation of a single red blood cell in bounded poiseuille flows. Phys. Rev. E, 85:016307, Jan 2012. doi: 10.1103/PhysRevE.85.016307. URL <https://link.aps.org/doi/10.1103/PhysRevE.85.016307>.
  - [48] C. Pozrikidis. Axisymmetric motion of a file of red blood cells through capillaries. Physics of Fluids, 17(3): 031503-031503-14, March 2005. doi: 10.1063/1.1830484.
  - [49] T. Omori, T. Ishikawa, D. Barthès-Biesel, A.-V. Salsac, Y. Imai, and T. Yamaguchi. Tension of red blood cell membrane in simple shear flow. Phys. Rev. E, 86:056321, Nov 2012. doi: 10.1103/PhysRevE.86.056321. URL <https://link.aps.org/doi/10.1103/PhysRevE.86.056321>.
  - [50] Chenghai Sun and Lance L. Munn. Lattice-boltzmann simulation of blood flow in digitized vessel networks. Computers & Mathematics with Applications, 55(7):1594 – 1600, 2008. ISSN 0898-1221. doi: <http://dx.doi.org/10.1016/j.camwa.2007.08.019>. Mesoscopic Methods in Engineering and Science.
  - [51] Kai-Chien Chang and Daniel A. Hammer. Influence of direction and type of applied force on the detachment of macromolecularly-bound particles from surfaces. Langmuir, 12(9):2271–2282, 1996. doi: 10.1021/la950690y. URL <https://doi.org/10.1021/la950690y>.
  - [52] Nipa A Mody and Michael R King. Influence of brownian motion on blood platelet flow behavior and adhesive dynamics near a planar wall. Langmuir : the ACS journal of surfaces and colloids, 23(11):6321–6328, 05 2007. doi: 10.1021/la0701475. URL <https://www.ncbi.nlm.nih.gov/pubmed/17417890>.
  - [53] Sean Fitzgibbon, Andrew P. Spann, Qin M. Qi, and Eric S.G. Shaqfeh. In vitro measurement of particle margination in the microchannel flow: Effect of varying hematocrit. Biophysical Journal, 108(10):2601 – 2608, 2015. ISSN 0006-3495. doi: <https://doi.org/10.1016/j.bpj.2015.04.013>. URL <http://www.sciencedirect.com/science/article/pii/S0006349515003914>.
  - [54] Kathrin Müller, Dmitry A. Fedosov, and Gerhard Gompper. Margination of micro- and nano-particles in blood flow and its effect on drug delivery. Scientific Reports, 4:4871 EP –, 05 2014. URL <https://doi.org/10.1038/srep04871>.
  - [55] Gang Ma, Jinsong Hua, and Hua Li. Numerical modeling of the behavior of an elastic capsule in a microchannel flow: The initial motion. Phys. Rev. E, 79:046710, Apr 2009. doi: 10.1103/PhysRevE.79.046710. URL

<https://link.aps.org/doi/10.1103/PhysRevE.79.046710>.

- [56] Junfeng Zhang, Paul C. Johnson, and Aleksander S. Popel. Effects of erythrocyte deformability and aggregation on the cell free layer and apparent viscosity of microscopic blood flows. Microvascular Research, 77(3):265 – 272, 2009. ISSN 0026-2862. doi: <https://doi.org/10.1016/j.mvr.2009.01.010>. URL <http://www.sciencedirect.com/science/article/pii/S0026286209000284>.
- [57] DMITRY A. FEDOSOV, BRUCE CASWELL, ALEKSANDER S. POPEL, and GEORGE EM KARNI-ADAKIS. Blood flow and cell-free layer in microvessels. Microcirculation, 17(8):615–628, 2010. doi: 10.1111/j.1549-8719.2010.00056.x. URL <https://onlinelibrary.wiley.com/doi/abs/10.1111/j.1549-8719.2010.00056.x>.
- [58] Margaret B. Fish, Catherine A. Fromen, Genesis Lopez-Cazares, Alexander W. Golinski, Timothy F. Scott, Rehemani Adili, Michael Holinstat, and Omolola Eniola-Adefeso. Exploring deformable particles in vascular-targeted drug delivery: Softer is only sometimes better. Biomaterials, 124:169 – 179, 2017. ISSN 0142-9612. doi: <https://doi.org/10.1016/j.biomaterials.2017.02.002>. URL <http://www.sciencedirect.com/science/article/pii/S0142961217300704>.



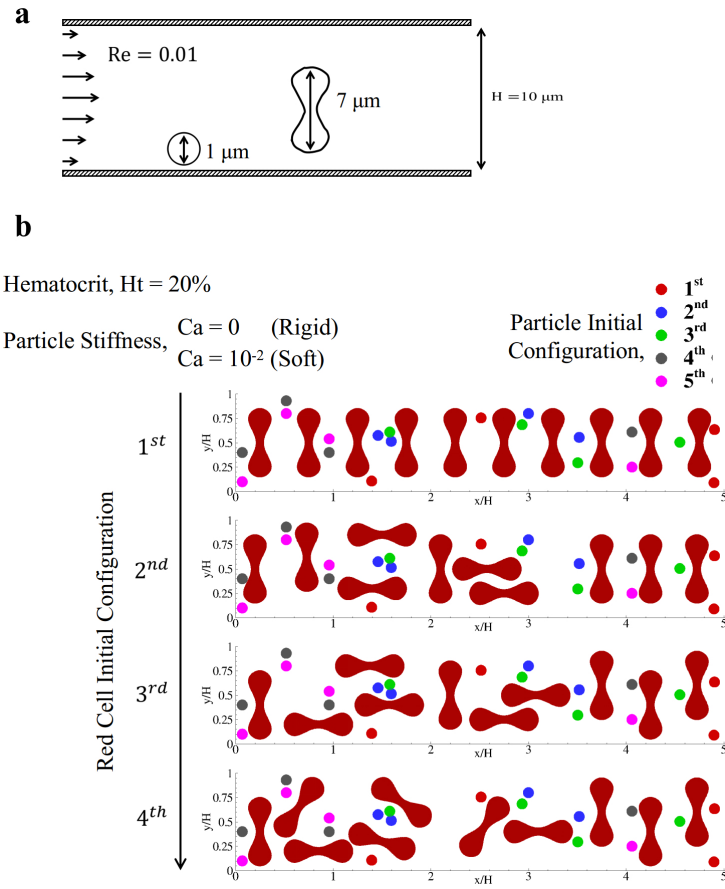


Figure 1: **Schematic of the physical problem.** **a.** Sketch of the computational domain with characteristic length and dimensions. **b.** The initial conditions for particles and red cells are obtained by choosing one per time the five particle initial positions within each of the four red blood cell configurations.

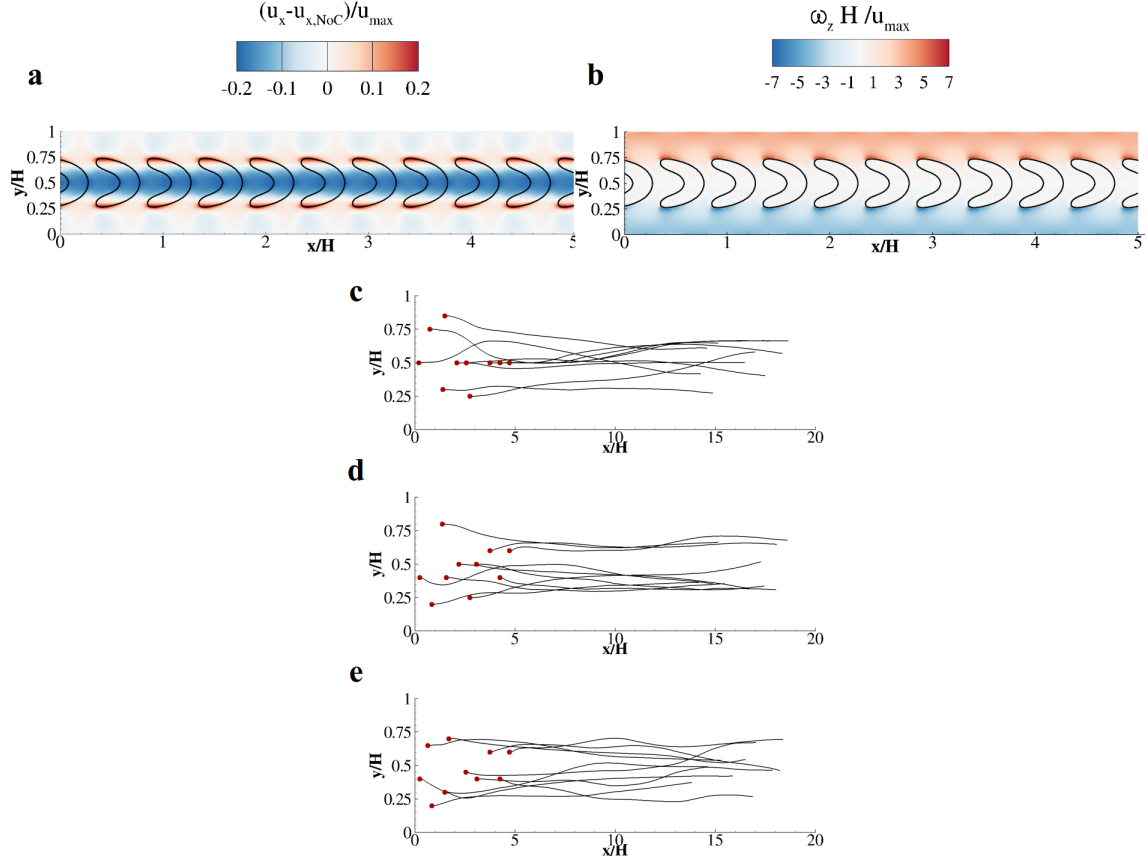


Figure 2: **Cell free layer formation in a  $10 \mu m$  high capillary with 20% hematocrit.** **a.** Contour plot of the linear slip velocity field along  $x$ ,  $\frac{u_x - u_{x,NoC}}{u_{max}}$ , taken at  $\frac{t u_{max}}{H} = 10$ , obtained with the initial single-filed RBC distribution. **b.** Contour plot of the out of plane vorticity,  $\frac{\omega_z H}{u_{max}}$ , taken at  $\frac{t u_{max}}{H} = 10$ , obtained with single-filed RBC distribution. **(c, d, e)** Trajectories of the center of mass obtained with the three disordered initial distribution of RBCs for  $0 < \frac{t u_{max}}{H} < 10$ .

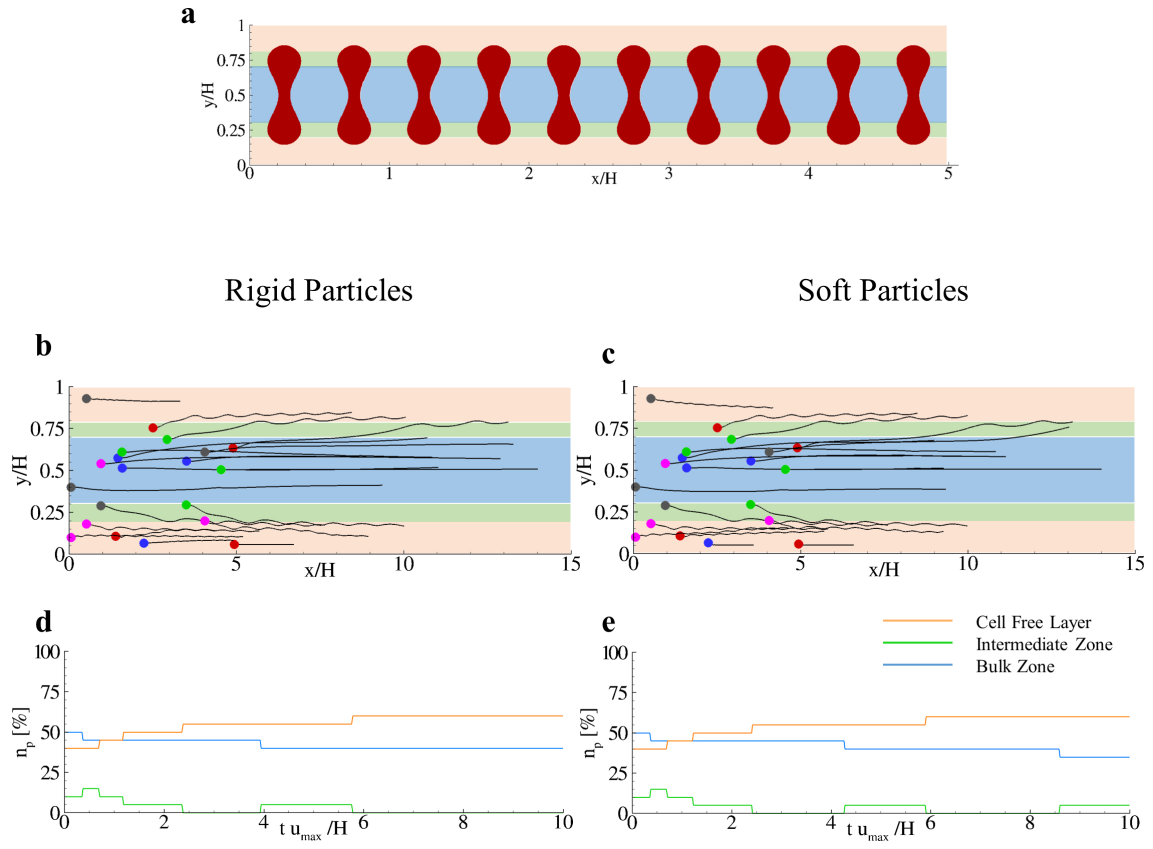


Figure 3: **Particle margination from a single-filed red blood cell initial distribution.** **a.** Red cell releasing positions in the computational domain. **(b, c)** Particle trajectories when transported as rigid membranes ( $Ca = 0$ ) and soft membranes ( $Ca = 10^{-2}$ ). **(d, e)** Number of particles populating the bulk zone, the intermediate zone and the cell-free layer over time.

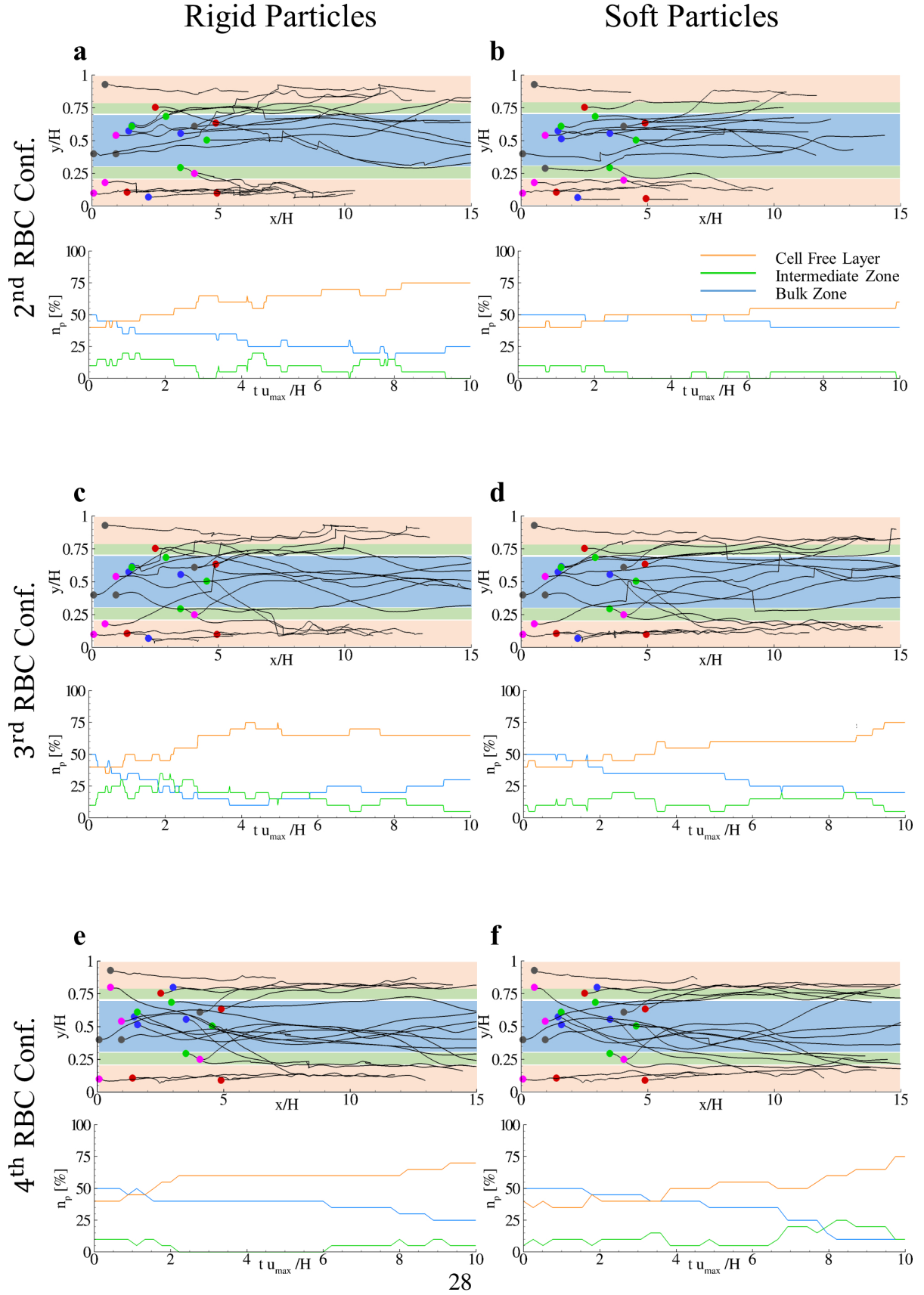


Figure 4: **Particle margination in three different red blood cell initial distributions.** Particle center of mass trajectories and number of particles in the bulk zone, the intermediate zone and the cell-free layer for rigid ( $Ca = 0$ ) and soft particles ( $Ca = 10^{-2}$ ) obtained with the second (a, b), third (c, d) and fourth (e, f) initial disordered configurations of red blood cells (see Figure.1).

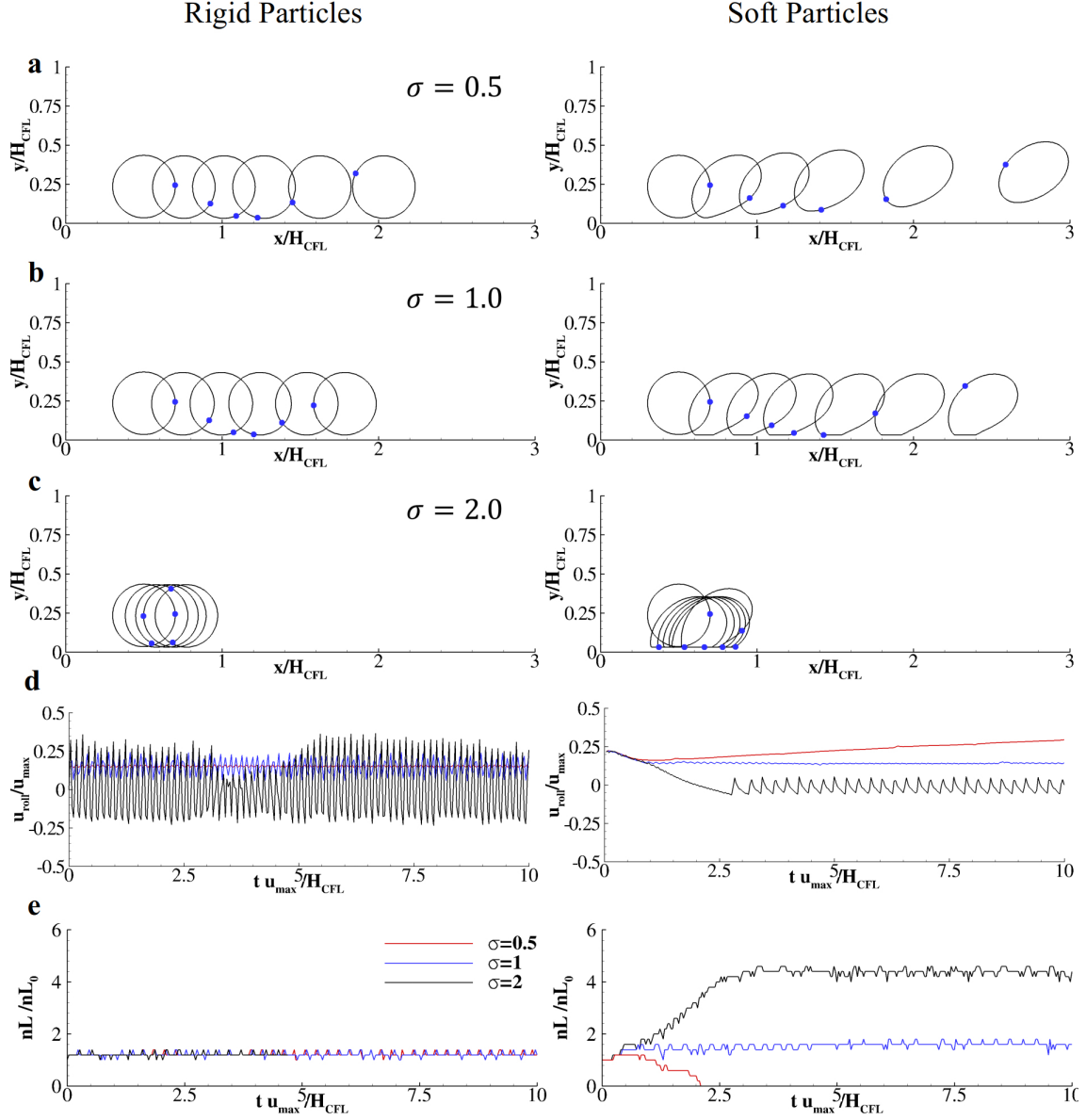


Figure 5: **Adhesion mechanics of rigid and soft particles navigating the cell free layer.** (a, b, c) Rigid and soft particles configurations representing the interaction with the vasculature for three different bonds strength ( $\sigma = 0.5, 1, \text{ and } 2$ ) taken at  $\frac{t u_{max}}{H} = 0, 1, 2, 3, 4, \text{ and } 5$ . (Blue dots are reference points for reader convenience.) **d.** Rolling velocity distribution of rigid (left) and soft (right) particles with  $\sigma = 0.5, 1.0, \text{ and } 2.0$ . **e.** Number of ligands activated during the transport of a representative rigid (left) and soft (right) particle with  $\sigma = 0.5, 1.0, \text{ and } 2.0$ .

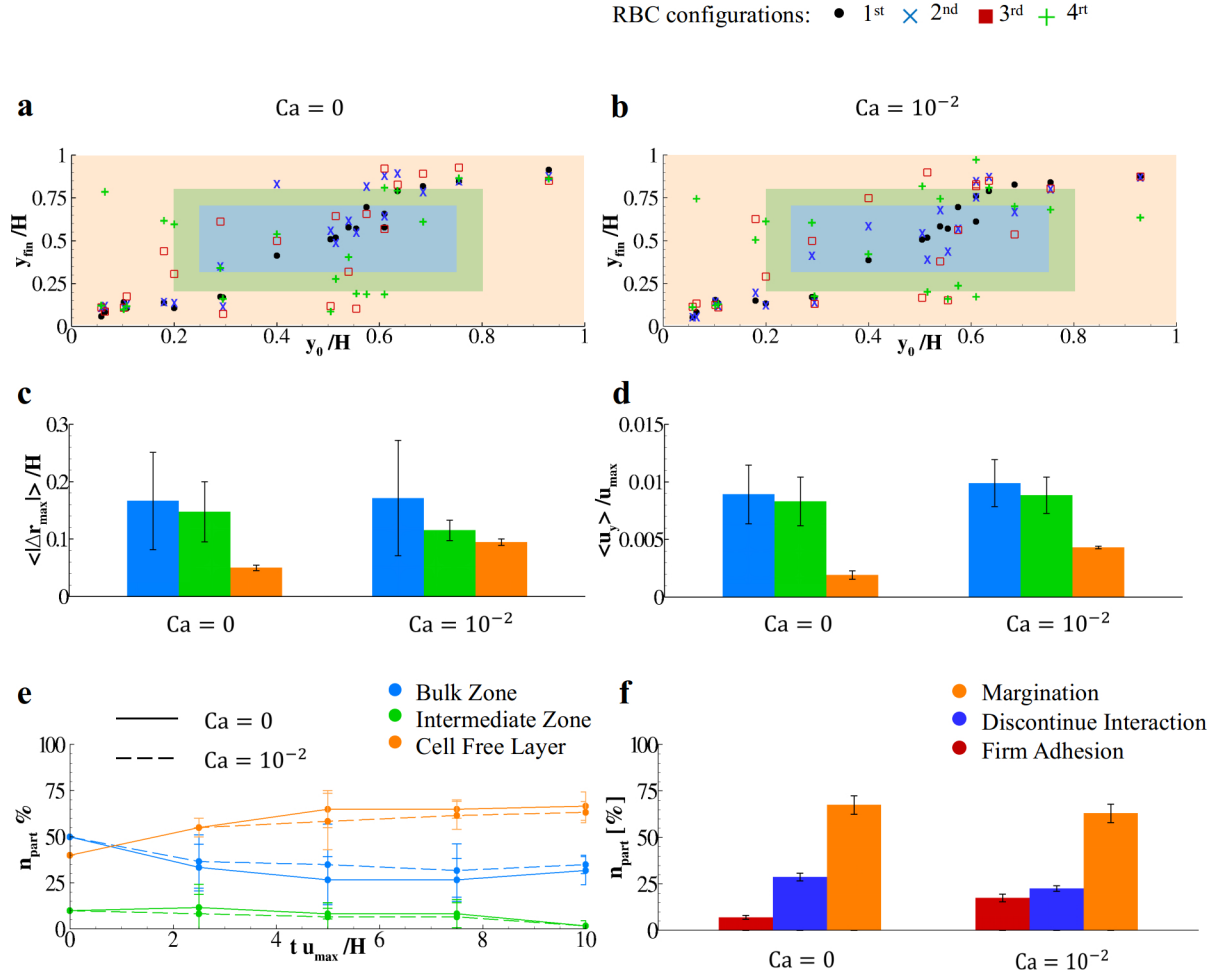


Figure 6: **Characterization of particle regimens in 10  $\mu\text{m}$  high blood capillaries.** (a, b) Plot of rigid (left) and soft (right) particle final lateral positions with respect to their releasing positions for the four different red blood cell initial configurations. (c, d) Module of the average maximum displacement exerted by the particles (both, rigid and soft) with respect to their releasing positions. (e) Mean particle lateral velocity classified with respect to particle releasing positions. (f) Number of particles in time populating the three different flow regions (bulk, intermediate and cell-free layer) averaged over the four red blood cell configurations. (g) Average number of firmly adhering, interacting with the vasculature (rolling or adhering) and marginating particles over the four different red blood cell configurations.